

# Visual Odometry Aided by a Sun Sensor and Inclinometer

Andrew Lambert, Paul Furgale, Timothy D. Barfoot

Institute for Aerospace Studies

University of Toronto

Toronto, ON M3H5T6

416-667-7700

{andrew.lambert,paul.furgale,tim.barfoot}@utoronto.ca

John Enright

Department of Aerospace Engineering

Ryerson University

Toronto, ON M5B2K3

416-979-5000x4174

jenright@ryerson.ca

**Abstract**—In this paper, we present a novel approach to localization for planetary rovers, in which sun sensor and inclinometer measurements are incorporated directly into a stereo visual odometry pipeline. Utilizing the absolute orientation information provided by the sun sensor significantly reduces the error growth of the visual odometry path estimate. The measurements have minimal computation, power, and mass requirements, providing a localization improvement at nearly negligible cost. We describe the mathematical formulation of error terms for the stereo camera, sun sensor, and inclinometer measurements, as well as the bundle adjustment framework for determining the maximum likelihood vehicle transformation. Improved localization accuracy is demonstrated through extensive experimental results from a 10 kilometre traversal of a Mars analogue site on Devon Island in the Canadian High Arctic.

## TABLE OF CONTENTS

<b>1 INTRODUCTION</b> .....	1
<b>2 PRIOR WORK</b> .....	2
<b>3 MATHEMATICAL FORMULATION</b> .....	2
<b>4 DESCRIPTION OF EXPERIMENTS</b> .....	8
<b>5 EXPERIMENTAL RESULTS</b> .....	9
<b>6 CONCLUSIONS</b> .....	12
<b>ACKNOWLEDGEMENTS</b> .....	12
<b>REFERENCES</b> .....	13
<b>BIOGRAPHY</b> .....	14

## 1. INTRODUCTION

During autonomous traverses across nominal terrain, the Mars Exploration Rovers (MERs) use wheel odometry measurements to track position changes of the vehicle, due to the absence of any satellite-based global positioning system (GPS) on Mars. However, the rovers have frequently encountered steep slopes and sandy terrain, resulting in large amounts of wheel slip and rendering the odometry measurements unreliable. For these high-slip situations, the MERs employ a technique called visual odometry (VO), where updated vehicle poses are determined by tracking keypoints between stereo image pairs. This method can provide accurate



**Figure 1.** The pushcart rover platform on Devon Island, a well-known planetary analogue site in the Canadian High Arctic.

localization in cases of wheel slip or wheel dragging, but can also act as an initial slip detection tool to increase vehicle safety [13]. The use of VO is currently limited to short drives due to computation time, but in future planetary missions with increased processor power, the benefits of visual odometry will be useful over longer range traverses. Unfortunately, the error of VO grows super-linearly with the distance travelled, primarily due to the contribution of orientation error [20].

To counteract this phenomenon, we have developed a novel approach incorporating sun sensor and inclinometer measurements directly into the VO pipeline to limit the error growth of our estimate. This approach was motivated by previous research demonstrating that periodic absolute orientation updates, such as those obtained from a sun sensor, restrict the error to grow only linearly with distance [20]. Note that the use of a sun sensor (or similarly a startracker) is well-suited for the exploration of Mars (or the Moon), whose lack of a useful magnetic field precludes the use of a compass for absolute heading information [4]. Additionally, a sun sensor is not subject to drift, which can plague inertial sensors used to monitor heading over long distances and times. The novel technique outlined in this paper builds upon this periodic ap-

<sup>1</sup> 978-1-4244-7351-9/11/\$26.00 ©2011 IEEE.

<sup>2</sup> IEEEAC Paper #1279, Version 2.0, Updated 09/01/2011.

proach, incorporating sun sensor and inclinometer measurements directly into the visual odometry solution as they are acquired. Our formulation allows for continuous correction of the vehicle’s heading estimate, allowing for greatly improved accuracy over long distances. The sun sensor provides absolute heading information (as well as pitch/roll over long periods of time), while the inclinometer measures the pitch and roll of the rover platform, allowing us to apply angular corrections to the full attitude of the vehicle.

The paper is organized as follows. First, we examine relevant prior work on visual odometry and review the use of sun sensors in rover navigation. Second, we outline the mathematical formulation of our estimation framework. Third, we provide the details of our experimental test data acquired at a Mars analog site on Devon Island in the Canadian Arctic. Finally, we provide the experimental results, and follow with conclusions and future work.

## 2. PRIOR WORK

The original visual odometry system was introduced by Moravec in 1980 [18]. The implementation was simple, but it was the first to contain the basic elements of the modern VO pipeline: a feature detector, a feature matcher, and a motion estimator. This basic model was continued by Matthies, who achieved significantly better accuracy by treating the motion estimation as a statistical estimation problem, and modelling the feature uncertainties as ellipsoidal three-dimensional Gaussians [16] [14].

The visual odometry system outlined by Matthies formed the basis of the MER algorithm [15], which we will examine in detail now. First, a pair of stereo images is acquired, and features are found in each image using the Harris corner detector [9]. Features are then matched across the stereo pair using pseudo-normalized cross-correlation [13]. After the rover moves a short distance, a second stereo pair is acquired, and features are matched across the two pairs. The locations of the features in the new images are predicted using a motion estimate from wheel odometry, reducing the search window. Next, a Random Sample Consensus (RANSAC) process is performed, which removes outliers and produces a coarse initial motion estimate using a closed-form least-squares calculation. Finally, a maximum likelihood estimation of the motion is iteratively computed, utilizing the three-dimensional covariances of the features [13].

A number of research labs have been investigating variations and extensions to this basic pipeline. Notable results have been obtained by Konolige et al. [12] at SRI International, who extend the visual odometry algorithm to include incremental sparse bundle adjustment (SBA). Features are detected using efficient Center Surround External (CenSurE) interest operator. The estimate errors are minimized by solving a sparse bundle adjustment over a handful of recent frames. Inertial Measurement Unit (IMU) data is fused with VO estimates using an EKF to minimize the long term positional

drift. Other notable systems have been developed by Mei et al. [17], Nister et al. [19], and Howard [10], among others.

The main focus of this paper is on using sun sensor and inclinometer measurements to aid visual odometry motion estimates. The inclusion of a sun sensor on future rover missions was one of the recommendations made after the 1997 Mars Pathfinder mission [23]. Subsequently, there were several studies at NASA’s Jet Propulsion Lab into the use of a dedicated sun sensor for rover navigation. A visual odometry simulation study by Olson et al. [20] found that long range position error grows super-linearly with the distance travelled, predominantly due to the contribution of orientation error. However, if absolute orientation measurements are available, the error is bounded to grow linearly with distance. Volpe [22] performed field tests using the Rocky 7 rover, in which wheel odometry motion estimates were corrected using a sun sensor, in conjunction with an accelerometer to determine sensor tilt. These tests experimentally verified that the use of an absolute orientation sensor restricts the positional error to grow linearly. Trebi-Ollenu et al. [21] describe the design and testing of a sun sensor on one of the FIDO rover platforms. Their sun sensor updates quickly with very little computation, but requires a complex precise calibration to avoid significant errors. Despite this research, the MER rovers actually use the PANCAM stereo camera pair to search for and acquire images of the sun [4]. This sun sensing technique is only used as a periodic heading or attitude update, not a direct component of any online navigation algorithm. This sun sensing procedure had only been used about 100 times as of January 2007 [13].

More recently, Enright et al. [5] presented an experimental study of sun sensing as a rover navigational aid. Navigational information is estimated using sun measurements, a local clock, quasi-analytical models of solar ephemeris, and, in some cases, a gravity vector measurement from an inclinometer. An estimate utilizing multiple measurements is determined by minimizing a scalar weighted cost function. Using these techniques, the absolute heading of the rover was able to be determined within a few degrees.

In summary, while significant research has been focused on visual odometry and sun sensor aided navigation, the algorithm presented in this paper is the first to incorporate sun sensor measurements directly into the visual odometry formulation. This novel approach provides considerable benefits for planetary rover exploration, as detailed in the following sections.

## 3. MATHEMATICAL FORMULATION

In this section, we outline the mathematical formulation of our visual odometry solution with sun sensor and inclinometer measurements. We start by establishing notational and mathematical conventions and defining our key coordinate frames. We then outline the derivation of the error terms for the stereo camera, sun sensor and inclinometer. Finally, we

discuss the bundle adjustment formulation that allows us to incorporate sun sensor and inclinometer measurements into the estimation solution as they are acquired. This approach enables us to constantly correct the orientation estimate of VO using absolute orientation information, preventing super-linear growth of error.

### Preliminaries

For the sake of clarity, we will briefly outline the notational scheme used in this paper. Vectors are represented by boldface lowercase characters, and matrices by boldface uppercase characters. The identity matrix is represented by  $\mathbf{1}$ , while a zero matrix is written as  $\mathbf{0}$ . An overbar denotes the nominal value of a quantity, while a hat over top of an element indicates that it is an estimate of a true quantity. The vector  $\rho_a^{d,e}$  represents a translation from point  $\mathbf{e}$  to point  $\mathbf{d}$ , expressed in coordinate frame  $\mathcal{F}_a$ . The rotation matrix  $\mathbf{C}_{a,b}$  rotates vectors expressed in  $\mathcal{F}_b$  into  $\mathcal{F}_a$ . We use the following set of three standard rotations, using the shorthand  $c_\theta \equiv \cos \theta$  and  $s_\theta \equiv \sin \theta$ :

$$\begin{aligned}\mathbf{R}_x(\theta) &= \begin{bmatrix} 1 & 0 & 0 \\ 0 & c_\theta & s_\theta \\ 0 & -s_\theta & c_\theta \end{bmatrix} \\ \mathbf{R}_y(\theta) &= \begin{bmatrix} c_\theta & 0 & -s_\theta \\ 0 & 1 & 0 \\ s_\theta & 0 & c_\theta \end{bmatrix} \\ \mathbf{R}_z(\theta) &= \begin{bmatrix} c_\theta & s_\theta & 0 \\ -s_\theta & c_\theta & 0 \\ 0 & 0 & 1 \end{bmatrix}\end{aligned}$$

Given any  $3 \times 1$  vector  $\mathbf{r} = [r_1 \ r_2 \ r_3]^T$ , we can also define the usual  $3 \times 3$  skew-symmetric cross operator [11]:

$$\mathbf{r}^\times := \begin{bmatrix} 0 & -r_3 & r_2 \\ r_3 & 0 & -r_1 \\ -r_2 & r_1 & 0 \end{bmatrix}$$

We will now discuss notation for the linearization of rotations, which will be used extensively throughout this paper. Let us define a rotation matrix  $\mathbf{C}(\boldsymbol{\theta})$ , where  $\boldsymbol{\theta}$  is a  $3 \times 1$  column of Euler angles that define the rotation. A perturbation in this rotation matrix can be written as follows:

$$\mathbf{C}(\bar{\boldsymbol{\theta}} + \delta\boldsymbol{\theta}) \approx (\mathbf{1} - (\mathbf{S}(\bar{\boldsymbol{\theta}}) \delta\boldsymbol{\theta})^\times) \mathbf{C}(\bar{\boldsymbol{\theta}}) \quad (1a)$$

$$= (\mathbf{1} - \delta\phi^\times) \mathbf{C}(\bar{\boldsymbol{\theta}}) \quad (1b)$$

where  $\bar{\boldsymbol{\theta}}$  is the nominal value,  $\delta\boldsymbol{\theta}$  is the perturbation,  $\mathbf{S}(\bar{\boldsymbol{\theta}})$  is the matrix relating rotation vectors to Euler angles evaluated at the operating point, and  $\mathbf{C}(\bar{\boldsymbol{\theta}})$  is the rotation matrix at the operating point [1]. We note that this expression describes how a perturbation of a rotation matrix, corresponds to a perturbation of Euler angles,  $\bar{\boldsymbol{\theta}} + \delta\boldsymbol{\theta}$ .

### Important Coordinate Frames

Our estimation framework relies on four main coordinate frames, with which we can describe all of our measurements

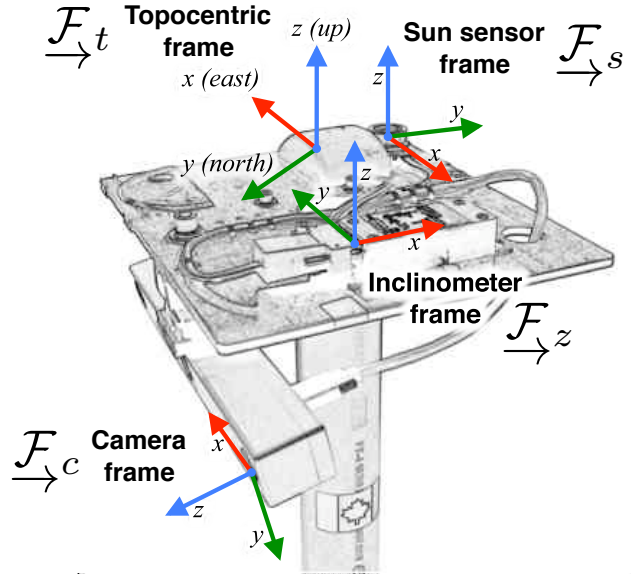


**Figure 2.** Illustration of the coordinate frames used in our formulation.

and vehicle transformations. Figure 2 shows the sensor head used in our experiments, with each of the relevant coordinates frames defined.

The camera frame,  $\mathcal{F}_c$ , is defined with origin at the left camera of the stereo apparatus. The  $x$ -axis is aligned with horizontal pixels, the  $y$ -axis with vertical pixels, and the  $z$ -axis is aligned with the optical axis. The sun sensor frame,  $\mathcal{F}_s$ , is defined having a  $z$ -axis aligned with the outward normal of the sensor. For the inclinometer frame,  $\mathcal{F}_g$ , the  $x$  and  $y$ -axes of the frame are defined by the orthogonal sensing axes of the sensor. The locally defined topocentric frame,  $\mathcal{F}_t$ , is such that the  $x$ -axis points in the eastward direction, the  $y$ -axis points north, and the  $z$ -axis is opposite to the local gravity vector.

With these definitions in hand, we can describe the pose of our rover. The estimate frame in our formulation,  $\mathcal{F}_{t_0}$ , has the orientation of the topocentric frame and is located at the origin of our GPS unit at time  $t = 0$ . At each time step  $k$ , we calculate the translation,  $\rho_{t_0}^{c_k, t_0}$ , and rotation,  $\mathbf{C}_{c_k, t_0}$ , of the camera frame  $\mathcal{F}_c$  relative to  $\mathcal{F}_{t_0}$ , which can easily be transformed to a vehicle frame using calibration information.

### Derivation of Error Terms

Given the stereo camera, sun sensor, and inclinometer measurements recorded at time  $k$ , our goal is to determine the maximum likelihood camera transformation at this timestep. Our method is to use a bundle adjustment approach that will estimate the states,  $\{\mathbf{C}_{c_k, t_0}, \rho_{t_0}^{c_k, t_0}\}$  and  $\{\mathbf{C}_{c_{k-1}, t_0}, \rho_{t_0}^{c_{k-1}, t_0}\}$ , and the positions of the stereo camera landmarks  $\mathbf{p}_{t_0}^{j, t_0}$ . Unlike the standard VO approach, which solves for a relative transformation from time  $k-1$  to  $k$ , we solve simultaneously

for the states relative to  $\mathcal{F}_{t_0}$  at both time  $k-1$  and time  $k$ ; this is because our new sun sensor and inclinometer measurement error terms require a current estimate of the vehicle orientation relative to the topocentric frame. In this technique, Gauss-Newton optimization is used to minimize an objective function composed of Mahalanobis distances proportional to the negative log likelihood of all the measurements. In order to build this objective function, we require error terms for each of the individual sensors, which we will derive in detail in this section.

**Stereo Camera Model**—We will now describe the observation models for our sensors, beginning with a stereo camera model. Note that we are not performing multi-frame visual odometry in this paper, but instead only matching stereo keypoints frame to frame, as on the MERs. Accordingly, we begin with an initial stereo image pair at time  $k-1$ , and then a second at time  $k$ . Our goal is to determine the translation and rotation of the camera between the two image pairs by estimating the two states,  $\{\mathbf{C}_{c_k, t_0}, \boldsymbol{\rho}_{t_0}^{c_k, t_0}\}$  and  $\{\mathbf{C}_{c_{k-1}, t_0}, \boldsymbol{\rho}_{t_0}^{c_{k-1}, t_0}\}$ . Our measurements are  $(u_l, v_l)$  and  $(u_r, v_r)$ , the pixel locations of observed keypoints in the left and right stereo images, respectively. The projection of landmark  $i$ , with three-dimensional location  $\mathbf{p}_{c_k}^{j, c_k} = [x \ y \ z]^T$ , into the image plane is described by our observation model for a stereo camera:

$$\mathbf{y}_k^j = \mathbf{h}(\mathbf{p}_{c_k}^{j, c_k}) = \begin{bmatrix} u_l \\ v_l \\ u_r \\ v_r \end{bmatrix} = \frac{1}{z} \begin{bmatrix} f_u x \\ f_v y \\ f_u(x-b) \\ f_v y \end{bmatrix} + \begin{bmatrix} c_u \\ c_v \\ c_u \\ c_v \end{bmatrix} + \delta \mathbf{y}_k^i$$

where  $f_u$  and  $f_v$  are the horizontal and vertical focal lengths,  $b$  is the camera baseline, and  $\delta \mathbf{y}_k^j$  is the noise associated with each measurement, modelled as a zero-mean Gaussian density with covariance  $\mathbf{T}_{y_k^j}$ . Thus, we can define the error term for stereo measurements as follows:

$$\mathbf{e}_{y_k}^j = \mathbf{y}_k^j - \mathbf{h}(\mathbf{p}_{c_k}^{j, c_k}) \quad (2)$$

The three-dimensional location of the landmark relative to the camera frame at time  $k$ ,  $\mathbf{p}_{c_k}^{j, c_k}$ , can be expressed as follows:

$$\mathbf{p}_{c_k}^{j, c_k} = \mathbf{C}_{c_k, t_0} (\bar{\mathbf{p}}_{t_0}^{j, t_0} - \bar{\boldsymbol{\rho}}_{t_0}^{c_k, t_0}) \quad (3)$$

In order to linearize the error term (2), we first perturb the feature location (3) about its nominal value, as follows:

$$\begin{aligned} \mathbf{p}_{c_k}^{j, c_k} &= \bar{\mathbf{p}}_{c_k}^{j, c_k} + \delta \mathbf{p}_{c_k}^{j, c_k} \\ &\approx (\mathbf{I} - \delta \phi_k^\times) \bar{\mathbf{C}}_{c_k, t_0} (\bar{\mathbf{p}}_{t_0}^{j, t_0} + \delta \mathbf{p}_{t_0}^{j, t_0} - \bar{\boldsymbol{\rho}}_{t_0}^{c_k, t_0} - \delta \boldsymbol{\rho}_{t_0}^{c_k, t_0}) \end{aligned}$$

Expanding and eliminating the products of small perturbation terms gives

$$\begin{aligned} \mathbf{p}_{c_k}^{j, c_k} &\approx \bar{\mathbf{C}}_{c_k, t_0} (\bar{\mathbf{p}}_{t_0}^{j, t_0} - \bar{\boldsymbol{\rho}}_{t_0}^{c_k, t_0}) + \bar{\mathbf{C}}_{c_k, t_0} \delta \mathbf{p}_{t_0}^{j, t_0} - \bar{\mathbf{C}}_{c_k, t_0} \delta \boldsymbol{\rho}_{t_0}^{c_k, t_0} \\ &\quad - \delta \phi_k^\times \bar{\mathbf{C}}_{c_k, t_0} \bar{\mathbf{p}}_{t_0}^{j, t_0} + \delta \phi_k^\times \bar{\mathbf{C}}_{c_k, t_0} \bar{\boldsymbol{\rho}}_{t_0}^{c_k, t_0}. \end{aligned}$$

Using the identity  $\mathbf{a}^\times \mathbf{b} = -\mathbf{b}^\times \mathbf{a}$ , we can rewrite the perturbed feature position as

$$\begin{aligned} \mathbf{p}_{c_k}^{j, c_k} &\approx \bar{\mathbf{C}}_{c_k, t_0} (\bar{\mathbf{p}}_{t_0}^{j, t_0} - \bar{\boldsymbol{\rho}}_{t_0}^{c_k, t_0}) + \bar{\mathbf{C}}_{c_k, t_0} \delta \mathbf{p}_{t_0}^{j, t_0} - \bar{\mathbf{C}}_{c_k, t_0} \delta \boldsymbol{\rho}_{t_0}^{c_k, t_0} \\ &\quad + \left[ (\bar{\mathbf{C}}_{c_k, t_0} \bar{\mathbf{p}}_{t_0}^{j, t_0})^\times - (\bar{\mathbf{C}}_{c_k, t_0} \bar{\boldsymbol{\rho}}_{t_0}^{c_k, t_0})^\times \right] \delta \phi_k. \end{aligned}$$

We can also apply the identity  $(\mathbf{C}\mathbf{r})^\times \equiv \mathbf{C}\mathbf{r}^\times \mathbf{C}^T$  to simplify the expression to

$$\begin{aligned} \mathbf{p}_{c_k}^{j, c_k} &\approx \bar{\mathbf{C}}_{c_k, t_0} (\bar{\mathbf{p}}_{t_0}^{j, t_0} - \bar{\boldsymbol{\rho}}_{t_0}^{c_k, t_0}) + \bar{\mathbf{C}}_{c_k, t_0} \delta \mathbf{p}_{t_0}^{j, t_0} - \bar{\mathbf{C}}_{c_k, t_0} \delta \boldsymbol{\rho}_{t_0}^{c_k, t_0} \\ &\quad + \bar{\mathbf{C}}_{c_k, t_0} (\bar{\mathbf{p}}_{t_0}^{j, t_0} - \bar{\boldsymbol{\rho}}_{t_0}^{c_k, t_0})^\times \bar{\mathbf{C}}_{c_k, t_0}^T \delta \phi_k. \end{aligned}$$

This equation can be written in matrix form as

$$\mathbf{p}_{c_k}^{j, c_k} = \bar{\mathbf{p}}_{c_k}^{j, c_k} + [\mathbf{D}_x^k \ \mathbf{D}_p^k] \begin{bmatrix} \delta \mathbf{x} \\ \delta \mathbf{p} \end{bmatrix}, \quad (4)$$

where

$$\mathbf{D}_x^k = \begin{bmatrix} \mathbf{0} & \mathbf{0} & -\bar{\mathbf{C}}_{c_k, t_0} & \bar{\mathbf{C}}_{c_k, t_0} (\bar{\mathbf{p}}_{t_0}^{j, t_0} - \bar{\boldsymbol{\rho}}_{t_0}^{c_k, t_0})^\times \bar{\mathbf{C}}_{c_k, t_0}^T \end{bmatrix},$$

$$\delta \mathbf{x} = \begin{bmatrix} \delta \boldsymbol{\rho}_{t_0}^{c_{k-1}, t_0} \\ \delta \phi_{k-1} \\ \delta \boldsymbol{\rho}_{t_0}^{c_k, t_0} \\ \delta \phi_k \end{bmatrix}, \quad \mathbf{D}_p^k = \bar{\mathbf{C}}_{c_k, t_0}, \quad \delta \mathbf{p} = \delta \mathbf{p}_{t_0}^{j, t_0}.$$

Substituting (4) into (2), we obtain our linearized error term:

$$\begin{aligned} \mathbf{e}_{y_k}^j &\approx \mathbf{y}_k^j - \mathbf{h}(\bar{\mathbf{p}}_{c_k}^{j, c_k} + [\mathbf{D}_x^k \ \mathbf{D}_p^k] \begin{bmatrix} \delta \mathbf{x} \\ \delta \mathbf{p} \end{bmatrix}) \\ &= \mathbf{y}_k^j - \mathbf{h}(\bar{\mathbf{p}}_{c_k}^{j, c_k}) + \frac{\partial \mathbf{h}}{\partial \mathbf{p}} \bigg|_{\bar{\mathbf{p}}_{c_k}^{j, c_k}} [\mathbf{D}_x^k \ \mathbf{D}_p^k] \begin{bmatrix} \delta \mathbf{x} \\ \delta \mathbf{p} \end{bmatrix} \\ &= \mathbf{y}_k^j - \mathbf{h}(\bar{\mathbf{p}}_{c_k}^{j, c_k}) + [\mathbf{A}_k^j \ \mathbf{B}_k^j] \begin{bmatrix} \delta \mathbf{x} \\ \delta \mathbf{p} \end{bmatrix} \quad (5) \end{aligned}$$

Following the same logical progression, an analogous error term can be derived for the same landmark observed at time  $k-1$ , which will depend on the state perturbation terms  $\delta \boldsymbol{\rho}_{t_0}^{c_{k-1}, t_0}$  and  $\delta \phi_{k-1}$ . The error term can be written as

$$\mathbf{e}_{y_{k-1}}^j = \mathbf{y}_{k-1}^j - \mathbf{h}(\bar{\mathbf{p}}_{c_{k-1}}^{j, c_{k-1}}) + [\mathbf{A}_{k-1}^j \ \mathbf{B}_{k-1}^j] \begin{bmatrix} \delta \mathbf{x} \\ \delta \mathbf{p} \end{bmatrix} \quad (6)$$

where

$$\mathbf{A}_{k-1}^j = \mathbf{E}_{k-1} \mathbf{D}_x^{k-1}, \quad \mathbf{B}_{k-1}^j = \mathbf{E}_{k-1} \bar{\mathbf{C}}_{c_{k-1}, t_0},$$

$$\mathbf{E}_{k-1} = \frac{\partial \mathbf{h}}{\partial \mathbf{p}} \bigg|_{\bar{\mathbf{p}}_{c_{k-1}}^{j, c_{k-1}}},$$

$$\mathbf{D}_x^{k-1} = \begin{bmatrix} -\bar{\mathbf{C}}_{c_{k-1}, t_0} & \bar{\mathbf{C}}_{c_{k-1}, t_0} (\bar{\mathbf{p}}_{t_0}^{j, t_0} - \bar{\boldsymbol{\rho}}_{t_0}^{c_{k-1}, t_0})^\times \bar{\mathbf{C}}_{c_{k-1}, t_0}^T & \mathbf{0} & \mathbf{0} \end{bmatrix}.$$

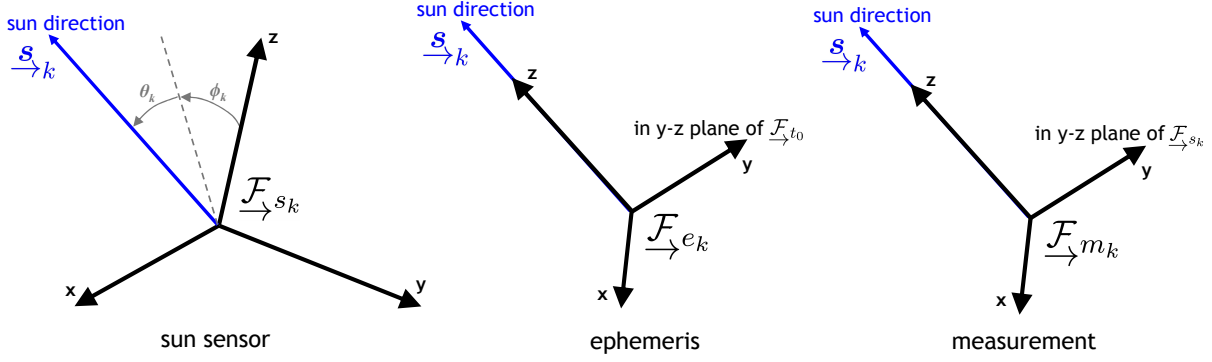


**Figure 3.** Definitions of the sun sensor measurements angle  $\phi_k$  and  $\theta_k$ , as well as the ephemeris and measurement frames.

*Sun Sensor Model*—We will now outline the derivation of the sun sensor observation model, which closely resembles the one derived by Barfoot et al [1]. After image acquisition and some post-processing, the sun sensor determines a unit vector pointing from the sensor to the sun. This unit vector can be completely described relative to the sun sensor frame by the measurement  $\mathbf{s}_k$ , consisting of a rotation about the  $x$ -axis by angle  $\phi_k$  and a rotation about the  $y$ -axis by  $\theta_k$ . The definition of these angles is shown in Figure 3. In order to perform our analysis, we also define an ephemeris frame  $\mathcal{F}_{e_k}$ , with  $z$ -axis aligned with the sun direction  $\mathbf{s}_k$  and  $y$ -axis lying in the  $y$ - $z$  plane of the topocentric frame  $\mathcal{F}_{t_0}$ . Additionally, we define a measurement frame  $\mathcal{F}_{m_k}$ , with  $z$ -axis aligned with the sun direction  $\mathbf{s}_k$  and  $y$ -axis lying in the  $y$ - $z$  plane of the sun sensor frame  $\mathcal{F}_{s_k}$ .

Thus, we can write the set of Euler angles from our current measurement,  $\tilde{\boldsymbol{\eta}}$ , as follows:

$$\mathbf{s}_k := \tilde{\boldsymbol{\eta}} = \begin{bmatrix} \theta_k \\ \phi_k \end{bmatrix} \quad (7)$$

Based on these angle definitions, we can define the following Euler sequence for  $\mathbf{C}_{s_k, m_k}$ , our measurement:

$$\mathbf{C}_{s_k, m_k} = \mathbf{R}_x(\phi_k) \mathbf{R}_y(\theta_k) \mathbf{R}_z(0) \quad (8)$$

We can also define an Euler sequence for  $\mathbf{C}_{e_k, m_k}$ , which is a rotation about the  $z$ -axis (of either frame) through an unknown angle,  $\psi_k$ :

$$\mathbf{C}_{e_k, m_k} = \mathbf{R}_x(0) \mathbf{R}_y(0) \mathbf{R}_z(\psi_k) \quad (9)$$

With these definitions at hand, we can now go about deriving an error term for the sun sensor measurements. Noting that  $\mathbf{C}_{s_k, m_k}$  contains the measurement information, we wish to build a predicted version of this,  $\hat{\mathbf{C}}_{s_k, m_k}$ . This predicted measurement will be based on our current attitude estimate relative to the topocentric frame,  $\hat{\mathbf{C}}_{c_k, t_0}$ , and the other inter-frame rotations:

$$\begin{aligned} \hat{\mathbf{C}}_{s_k, m_k} &:= \mathbf{C}_{c, s}^T \hat{\mathbf{C}}_{c_k, t_0} \mathbf{C}_{t_0, e_k} \mathbf{C}_{e_k, m_k} \\ &= \mathbf{R}_x(\hat{\phi}_k) \mathbf{R}_y(\hat{\theta}_k) \mathbf{R}_z(\hat{\nu}_k) \end{aligned}$$

Note that the rotation,  $\mathbf{C}_{t_0, e_k}$ , can be obtained from ephemeris, date and time of day, and an approximate knowledge of our current global position, and thus can be considered a known quantity. Also, the rotation,  $\mathbf{C}_{c, s}$ , is the rotation between the sun sensor and camera frames, and is assumed to be known from calibration. The angle  $\hat{\nu}_k$  is non-zero because we are using  $\hat{\mathbf{C}}_{c_k, t_0}$ , not the true value,  $\mathbf{C}_{c_k, t_0}$ . Next, we can write the current timestep attitude estimate,  $\hat{\mathbf{C}}_{c_k, t_0}$ , as a multiplicative perturbation about some initial estimate,  $\bar{\mathbf{C}}_{c_k, t_0}$ , as follows:

$$\begin{aligned} \hat{\mathbf{C}}_{s_k, m_k} &\approx \mathbf{C}_{c, s}^T (\mathbf{I} - \delta\boldsymbol{\phi}^\times) \bar{\mathbf{C}}_{c_k, t_0} \mathbf{C}_{t_0, e_k} \mathbf{C}_{e_k, m_k} \\ &= \mathbf{C}_{c, s}^T \bar{\mathbf{C}}_{c_k, t_0} \mathbf{C}_{t_0, e_k} \mathbf{C}_{e_k, m_k} \\ &\quad - \mathbf{C}_{c, s}^T \delta\boldsymbol{\phi}^\times \bar{\mathbf{C}}_{c_k, t_0} \mathbf{C}_{t_0, e_k} \mathbf{C}_{e_k, m_k} \end{aligned}$$

Next, we insert the term  $\mathbf{C}_{c, s} \mathbf{C}_{c, s}^T$ , which is equal to identity, into the expression:

$$\begin{aligned} \hat{\mathbf{C}}_{s_k, m_k} &= \mathbf{C}_{c, s}^T \bar{\mathbf{C}}_{c_k, t_0} \mathbf{C}_{t_0, e_k} \mathbf{C}_{e_k, m_k} \\ &\quad - \mathbf{C}_{c, s}^T \delta\boldsymbol{\phi}^\times \mathbf{C}_{c, s} \mathbf{C}_{c, s}^T \bar{\mathbf{C}}_{c_k, t_0} \mathbf{C}_{t_0, e_k} \mathbf{C}_{e_k, m_k} \end{aligned}$$

Using the identity  $(\mathbf{C}\mathbf{r})^\times \equiv \mathbf{C}\mathbf{r}^\times \mathbf{C}^T$ , we can reduce the expression to the following:

$$\hat{\mathbf{C}}_{s_k, m_k} = \left[ \mathbf{I} - (\mathbf{C}_{c, s}^T \delta\boldsymbol{\phi})^\times \right] \mathbf{C}_{c, s}^T \bar{\mathbf{C}}_{c_k, t_0} \mathbf{C}_{t_0, e_k} \mathbf{C}_{e_k, m_k} \quad (10)$$

The compound rotation,  $\mathbf{C}_{c, s}^T \bar{\mathbf{C}}_{c_k, t_0} \mathbf{C}_{t_0, e_k}$ , may be expressed as the following Euler sequence:

$$\mathbf{C}_{c, s}^T \bar{\mathbf{C}}_{c_k, t_0} \mathbf{C}_{t_0, e_k} = \mathbf{R}_x(\bar{\phi}_k) \mathbf{R}_y(\bar{\theta}_k) \mathbf{R}_z(\bar{\nu}_k)$$

Thus, we can write (10) as follows:

$$\begin{aligned} \hat{\mathbf{C}}_{s_k, m_k} &= \left[ \mathbf{I} - (\mathbf{C}_{c, s}^T \delta\boldsymbol{\phi})^\times \right] \mathbf{R}_x(\bar{\phi}_k) \mathbf{R}_y(\bar{\theta}_k) \mathbf{R}_z(\bar{\nu}_k) \mathbf{R}_z(\psi_k) \\ &= \left[ \mathbf{I} - (\mathbf{C}_{c, s}^T \delta\boldsymbol{\phi})^\times \right] \mathbf{R}_x(\bar{\phi}_k) \mathbf{R}_y(\bar{\theta}_k) \mathbf{R}_z(\bar{\nu}_k + \psi_k) \\ &= \left[ \mathbf{I} - (\mathbf{C}_{c, s}^T \delta\boldsymbol{\phi})^\times \right] \bar{\mathbf{C}}_{s_k, m_k} \end{aligned} \quad (11)$$

where  $\bar{\mathbf{C}}_{s_k, m_k} = \mathbf{R}_x(\bar{\phi}_k) \mathbf{R}_y(\bar{\theta}_k) \mathbf{R}_z(\bar{\nu}_k + \psi_k)$ . The angle  $\psi_k$  is unknown, but as we will see, we will not need it. The



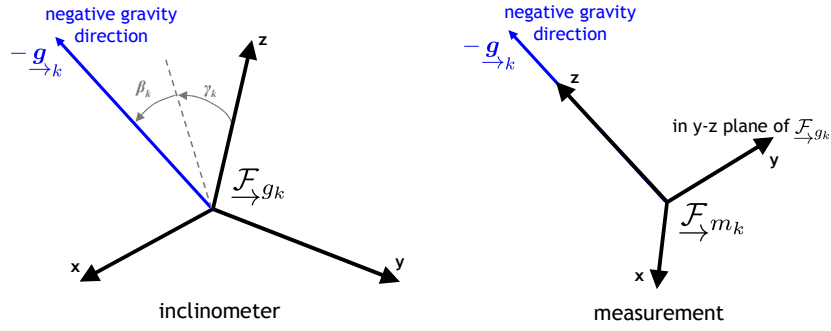


**Figure 4.** Definitions of the inclinometer measurements angle  $\beta_k$  and  $\gamma_k$ , as well as the measurement frame.

resulting expression for our predicted measurement is of the same linearized form as (1b), with the  $\delta\phi$  from (1b) taking the form  $\mathbf{C}_{c,s}^T \delta\phi$  in (11). Thus, the perturbation of the predicted measurement rotation matrix, as shown in (11), corresponds to a perturbation of the predicted measurement Euler angles,  $\hat{\eta} \approx \bar{\eta} + \delta\eta$ . We can derive an expression for the perturbation  $\delta\eta$  using (1a) and (1b):

$$\begin{aligned} \mathbf{C}_{c,s}^T \delta\phi &= \mathbf{S}(\bar{\eta}) \delta\eta \\ \Rightarrow \delta\eta &= \mathbf{S}^{-1}(\bar{\eta}) \mathbf{C}_{c,s}^T \delta\phi \end{aligned} \quad (12)$$

Thus, the expression for the perturbed predicted measurement in Euler angles is as follows:

$$\hat{\eta} = \bar{\eta} + \mathbf{S}^{-1}(\bar{\eta}) \mathbf{C}_{c,s}^T \delta\phi \quad (13)$$

where

$$\hat{\eta} := \begin{bmatrix} \hat{\nu}_k \\ \hat{\theta}_k \\ \hat{\phi}_k \end{bmatrix}, \quad (14)$$

$$\bar{\eta} := \begin{bmatrix} \bar{\nu}_k + \psi \\ \bar{\theta}_k \\ \bar{\phi}_k \end{bmatrix}, \quad (15)$$

$$\mathbf{S} := \begin{bmatrix} \mathbf{R}_x(\bar{\phi}) \mathbf{R}_y(\bar{\theta}) \mathbf{1}_3 & \mathbf{R}_x(\bar{\phi}) \mathbf{1}_2 & \mathbf{1}_1 \end{bmatrix}. \quad (16)$$

Note that the unknown angles  $\nu_k$  and  $\psi_k$  are not used in the calculation of  $\mathbf{S}$ , due to our selection of Euler sequence. Additionally, our selection of Euler sequence has its singularity at  $\theta_k = \pi/2$ , which is out of the field of view of our sensor. We note, however, that our Euler angle terms consist of 3 unique angles, while our measurements consist of only 2 angles. To put our error expression in the same terms as our measurements, we utilize a projection matrix,  $\mathbf{P}$ , of the following form:

$$\mathbf{P} := \begin{bmatrix} 0 & 1 & 0 \\ 0 & 0 & 1 \end{bmatrix}$$

Multiplying (13) by this projection matrix gives us the predicted sun sensor measurement in 2 Euler angles. Note that the application of the projection matrix makes the values of the unknown angles  $\nu_k$  and  $\psi_k$  irrelevant. We can now write our final linearized expression for the sun sensor measurement error:

$$\mathbf{e}_{s_k} = (\mathbf{s}_k - \hat{\eta}) = \mathbf{s}_k - \mathbf{P} \left( \bar{\eta} + \mathbf{S}^{-1}(\bar{\eta}) \mathbf{C}_{c,s}^T \delta\phi \right) \quad (17)$$

For clarity, we can describe the error term for the  $m^{\text{th}}$  sun vector measurement as follows:

$$\mathbf{e}_{s_k}^m = \mathbf{s}_k^m - \mathbf{P} \bar{\eta}_m + \mathbf{U}_m \delta\mathbf{x} \quad (18)$$

where

$$\mathbf{U}_m = \begin{bmatrix} \mathbf{0} & \mathbf{0} & \mathbf{0} & -\mathbf{S}^{-1}(\bar{\eta}_m) \mathbf{C}_{c,s}^T \end{bmatrix}.$$

*Inclinometer Model*—The process of deriving the inclinometer model is essentially the same as for the sun sensor, so we present a very brief summary of the main concepts here. The inclinometer is measuring the pitch angle  $\beta_k$  and roll angle  $\gamma_k$  of the inclinometer with respect to the topocentric frame. The definition of these angles is shown in Figure 4, where we have shown the angles measured relative to the negative gravity vector, which is equivalent to the negative  $z$ -axis of the topocentric frame. We also define a measurement frame  $\mathcal{F}_{m_k}$ , with  $z$ -axis aligned with the negative gravity direction  $\underline{g}_k$  and  $y$ -axis lying in the  $y$ - $z$  plane of the inclinometer frame  $\mathcal{F}_{g_k}$ . Thus, we can write the set of Euler angles from our current measurement,  $\tilde{\eta}$ , as follows:

$$\mathbf{g}_k := \tilde{\eta} = \begin{bmatrix} \beta_k \\ \gamma_k \end{bmatrix} \quad (19)$$

Based on these angle definitions, we can define the following Euler sequence for  $\mathbf{C}_{g_k, m_k}$ , our measurement:

$$\mathbf{C}_{g_k, m_k} = \mathbf{R}_x(\gamma_k) \mathbf{R}_y(\beta_k) \mathbf{R}_z(0)$$

We can also define a Euler sequence for  $\mathbf{C}_{t_0, m_k}$ , which is a rotation about the  $z$ -axis (of either frame) through an unknown angle,  $\psi_k$ :

$$\mathbf{C}_{t_0, m_k} = \mathbf{R}_x(0) \mathbf{R}_y(0) \mathbf{R}_z(\psi_k)$$

Noting that  $\mathbf{C}_{g_k, m_k}$  contains the measurement information, we can build a predicted version of this,  $\hat{\mathbf{C}}_{g_k, m_k}$ . This predicted measurement will be based on our current attitude estimate relative to the topocentric frame,  $\hat{\mathbf{C}}_{c_k, t_0}$ , and the other interframe rotations:

$$\hat{\mathbf{C}}_{g_k, m_k} := \mathbf{C}_{c, g}^T \hat{\mathbf{C}}_{c_k, t_0} \mathbf{C}_{t_0, m_k} = \mathbf{R}_x(\hat{\gamma}_k) \mathbf{R}_y(\hat{\beta}_k) \mathbf{R}_z(\hat{\nu}_k)$$

Following the same procedure as outlined in the sun sensor

model subsection, the linearized inclinometer error term can be determined from the above equations as follows:

$$\mathbf{e}_{g_k} = \mathbf{g}_k - \mathbf{P} \left( \bar{\boldsymbol{\eta}} - \mathbf{S}^{-1} (\bar{\boldsymbol{\eta}}) \mathbf{C}_{c,g}^T \delta \phi \right) \quad (20)$$

For clarity, we can describe the error term for the  $n^{\text{th}}$  inclinometer measurement as follows:

$$\mathbf{e}_{g_k}^n = \mathbf{g}_k^n - \mathbf{P} \bar{\boldsymbol{\eta}}_n + \mathbf{G}_n \delta \mathbf{x} \quad (21)$$

where

$$\mathbf{G}_n = \begin{bmatrix} \mathbf{0} & \mathbf{0} & \mathbf{0} & -\mathbf{S}^{-1} (\bar{\boldsymbol{\eta}}_n) \mathbf{C}_{c,g}^T \end{bmatrix}. \quad (22)$$

### Bundle Adjustment Solution

As previously mentioned, because our sun sensor and inclinometer measurement error terms require a current estimate of the vehicle orientation relative to the topocentric frame, we solve simultaneously for the states relative to  $\mathcal{F}_{t_0}$  at both time  $k-1$  and time  $k$ . To constrain this solution in space, we include a prior on the state variables based on the estimate up to the current time; this bundle adjustment implementation is functionally similar to the iterated extended Kalman filter.

Using our linearized error terms from above, we can construct our objective function, which we will minimize to obtain the maximum likelihood estimate for our new vehicle state:

$$\mathbf{J}_k(\mathbf{x}, \mathbf{p}) := \frac{1}{2} (\mathbf{e}_x^T \mathbf{T}_x^{-1} \mathbf{e}_x + \mathbf{e}_g^T \mathbf{T}_g^{-1} \mathbf{e}_g + \mathbf{e}_s^T \mathbf{T}_s^{-1} \mathbf{e}_s + \mathbf{e}_y^T \mathbf{T}_y^{-1} \mathbf{e}_y)$$

where

$$\mathbf{e}_x = \tilde{\mathbf{x}}_{k-1} - \bar{\mathbf{x}}_{k-1}$$

and where  $\tilde{\mathbf{x}}_{k-1}$  is the estimate of the state  $\{\mathbf{C}_{c_{k-1}, t_0}, \boldsymbol{\rho}_{t_0}^{c_{k-1}, t_0}\}$  resulting from the bundle adjustment estimation at the previous timestep, and  $\bar{\mathbf{x}}_{k-1}$  is our current estimate for the state  $\{\mathbf{C}_{c_{k-1}, t_0}, \boldsymbol{\rho}_{t_0}^{c_{k-1}, t_0}\}$  at this timestep. Additionally,  $\mathbf{T}_x^{-1}$ ,  $\mathbf{T}_g^{-1}$ ,  $\mathbf{T}_s^{-1}$ , and  $\mathbf{T}_y^{-1}$  represent the inverse covariance matrices for the previous state, inclinometer, sun sensor, and stereo feature measurements, respectively. We can minimize this objective function using Gauss-Newton optimization. An update step in the optimization process can be determined by augmenting the classic bundle adjustment update step as follows:

$$\mathbf{H}^T \mathbf{T}^{-1} \mathbf{H} \begin{bmatrix} \delta \mathbf{x} \\ \delta \mathbf{p} \end{bmatrix} = -\mathbf{H}^T \mathbf{T}^{-1} \mathbf{e}(\bar{\mathbf{x}}, \bar{\mathbf{p}}) \quad (23)$$

where

$$\mathbf{H} = \begin{bmatrix} \mathbf{R} & \mathbf{0} \\ \mathbf{G} & \mathbf{0} \\ \mathbf{U} & \mathbf{0} \\ \mathbf{A} & \mathbf{B} \end{bmatrix}, \quad \mathbf{T}^{-1} = \text{diag} \{ \mathbf{T}_x^{-1}, \mathbf{T}_g^{-1}, \mathbf{T}_s^{-1}, \mathbf{T}_y^{-1} \},$$

$$\mathbf{R} = \begin{bmatrix} \mathbf{1} & \mathbf{0} \end{bmatrix}, \quad \mathbf{e}(\bar{\mathbf{x}}, \bar{\mathbf{p}}) = \begin{bmatrix} \mathbf{e}_x \\ \mathbf{e}_g \\ \mathbf{e}_s \\ \mathbf{e}_y \end{bmatrix},$$

and where  $\mathbf{G}$  is a matrix combining the inclinometer Jacobians  $\mathbf{G}_n$  at this timestep,  $\mathbf{U}$  is a matrix combining the sun

sensor Jacobians  $\mathbf{U}_m$  at this timestep, while  $\mathbf{A}$  and  $\mathbf{B}$  incorporate each of the Jacobians  $\mathbf{A}_k^j$  and  $\mathbf{B}_k^j$  for the keypoints observed at time  $k$  as well as the Jacobians  $\mathbf{A}_{k-1}^j$  and  $\mathbf{B}_{k-1}^j$  for the same keypoints observed at the time  $k-1$ . Constructing the lefthand side, we have

$$\mathbf{H}^T \mathbf{T}^{-1} \mathbf{H} = \left[ \begin{array}{c|c} \mathbf{R}^T \mathbf{T}_x^{-1} \mathbf{R} + \mathbf{G}^T \mathbf{T}_g^{-1} \mathbf{G} + \mathbf{U}^T \mathbf{T}_s^{-1} \mathbf{U} + \mathbf{A}^T \mathbf{T}_y^{-1} \mathbf{A} & \mathbf{A}^T \mathbf{T}_y^{-1} \mathbf{B} \\ \hline \mathbf{B}^T \mathbf{T}_y^{-1} \mathbf{A} & \mathbf{B}^T \mathbf{T}_y^{-1} \mathbf{B} \end{array} \right]$$

where the matrix is partitioned into the pose and landmark components. We can explicitly illustrate the contributions of the stereo camera, prior, sun sensor, and inclinometer terms by rewriting (24) as a sum:

$$\mathbf{H}^T \mathbf{T}^{-1} \mathbf{H} = \underbrace{\left[ \begin{array}{c|c} \mathbf{A}^T \mathbf{T}_y^{-1} \mathbf{A} & \mathbf{A}^T \mathbf{T}_y^{-1} \mathbf{B} \\ \hline \mathbf{B}^T \mathbf{T}_y^{-1} \mathbf{A} & \mathbf{B}^T \mathbf{T}_y^{-1} \mathbf{B} \end{array} \right]}_{\text{stereo camera terms}} + \underbrace{\left[ \begin{array}{c|c} \mathbf{R}^T \mathbf{T}_x^{-1} \mathbf{R} + \mathbf{G}^T \mathbf{T}_g^{-1} \mathbf{G} + \mathbf{U}^T \mathbf{T}_s^{-1} \mathbf{U} & \mathbf{0} \\ \hline \mathbf{0} & \mathbf{0} \end{array} \right]}_{\text{prior, sun sensor, and inclinometer terms}} \quad (24)$$

From (24), we can see that the inclusion of the additional measurements does not disturb the sparse structure of the bundle adjustment problem. The prior, sun sensor, and inclinometer terms are block diagonal, and are added to the upper left corner of the stereo camera terms, which is also block diagonal. Thus, the sparse structure is preserved, allowing computationally-efficient sparse methods to be used for solving [3].

We determine the state at time  $k$ ,  $\{\mathbf{C}_{c_k, t_0}, \boldsymbol{\rho}_{t_0}^{c_k, t_0}\}$ , through an iterative process:

1. Using the current estimated values for  $\{\mathbf{C}_{c_k, t_0}, \boldsymbol{\rho}_{t_0}^{c_k, t_0}\}$ ,  $\{\mathbf{C}_{c_{k-1}, t_0}, \boldsymbol{\rho}_{t_0}^{c_{k-1}, t_0}\}$ , and  $\mathbf{p}_{t_0}^{j, t_0}$ , compute an update step  $[\delta \mathbf{x}^T \quad \delta \mathbf{p}^T]^T$  by solving equation (23) using sparse bundle adjustment methods.
2. Check for convergence. If converged, stop; otherwise continue to Step 3.
3. The state and feature position updates are then applied to  $\{\mathbf{C}_{c_k, t_0}, \boldsymbol{\rho}_{t_0}^{c_k, t_0}\}$ ,  $\{\mathbf{C}_{c_{k-1}, t_0}, \boldsymbol{\rho}_{t_0}^{c_{k-1}, t_0}\}$ , and  $\mathbf{p}_{t_0}^{j, t_0}$ , respectively, according to

$$\begin{aligned} \mathbf{C}_{c_k, t_0} &\leftarrow \Phi_k \mathbf{C}_{c_k, t_0}, \\ \boldsymbol{\rho}_{t_0}^{c_k, t_0} &\leftarrow \boldsymbol{\rho}_{t_0}^{c_k, t_0} + \delta \boldsymbol{\rho}_{t_0}^{c_k, t_0}, \\ \mathbf{p}_{t_0}^{j, t_0} &\leftarrow \mathbf{p}_{t_0}^{j, t_0} + \delta \mathbf{p}_{t_0}^{j, t_0}, \end{aligned}$$

where

$$\begin{aligned} \Phi_k &= \cos(\delta \phi_k) \mathbf{1} + (1 - \cos(\delta \phi_k)) \left( \frac{\delta \phi_k}{\delta \phi_k} \right) \left( \frac{\delta \phi_k}{\delta \phi_k} \right)^T \\ &\quad - \sin(\delta \phi_k) \left( \frac{\delta \phi_k}{\delta \phi_k} \right)^\times, \end{aligned}$$

and  $\delta \phi_k := |\delta \phi_k|$ .

4. Return to Step 1.

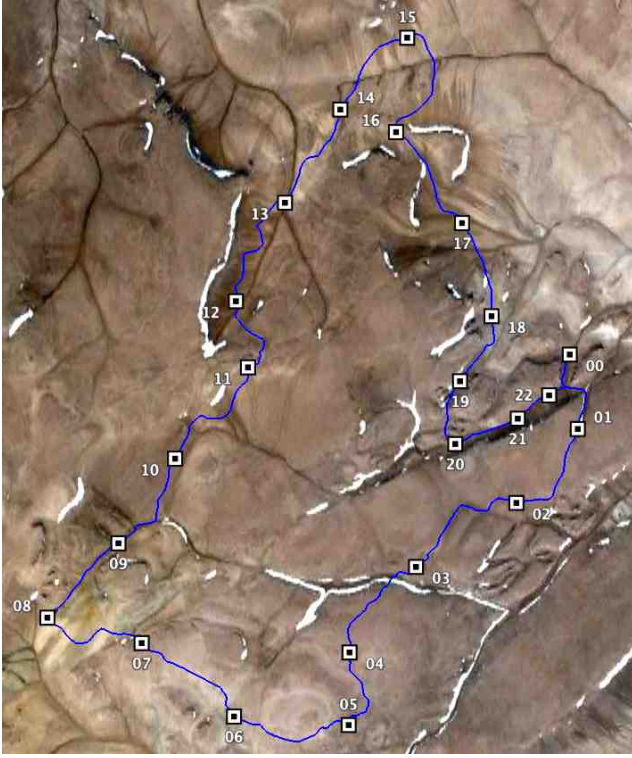


**Figure 5.** The 10 km traverse loop plotted in Google Earth, with the starting points for the 23 individual sections shown.

Note that while we solve for the previous state at time  $k - 1$  as part of bundle adjustment, the converged solution is essentially identical to our previous estimate, so the new estimate is discarded (it was necessary only to allow the incorporation of the sun sensor and inclinometer measurements).

This formulation allows us to incorporate sun sensor and inclinometer measurements directly into the visual odometry solution, as we acquire them. Note that we do not require both or any sun vector and gravity measurements at a given time step; any measurements that are available can be individually included in the bundle adjustment solution. Thus, whenever possible, we are continuously correcting the camera orientation using absolute information, preventing the aggregation of errors over time. If there are no absolute orientation measurements at that time step, the bundle adjustment will proceed as usual, solving for the camera transformation using only the stereo keypoints.

#### 4. DESCRIPTION OF EXPERIMENTS

In order to test our visual odometry algorithm with sun sensor and inclinometer measurements, extensive data were collected during a 10 km rover traverse in a Mars analog environment on Devon Island. The recorded data have been processed and packaged into a complete data set [8], including stereo images, sun vectors, inclinometer gravity vectors, and GPS groundtruth for position. The details of this data set are presented in this section, including particulars of the traverse and the hardware configuration.



**Figure 6.** Typical images acquired by the stereo camera during the 10 km traverse of Devon Island. For our experiments, we used  $512 \times 384$  greyscale versions of the images.

#### Scenario Description

Our data collection took place near the Houghton-Mars Project Research Station (HMPRS) ( $75^{\circ}22'$  N latitude and  $89^{\circ}41'$  W longitude) on Devon Island in the Canadian High Arctic. The site is considered to be a strong analog for planetary environments [2] due to its geological makeup and vegetation-free desert landscape, as seen in Figures 1 and 4. A pushcart rover platform traversed a 10 km loop through rugged canyons, sandy flats, and high-grade slopes over a period of 10 hours. To illustrate the path of the pushcart rover, Figure 5 shows the entire traverse loop plotted in Google Earth. The test was performed in July 2008; the Arctic sun remained above the horizon line for 24 hours a day.

The 10 km loop has been partitioned into 23 sections of varying length, labelled with indices from 0 to 22. For the purposes of error reporting for the individual traverse sections, we have aligned the first 50 m of each estimated section path with the GPS groundtruth path, and then calculated the error on the remaining length of the traverse. Positional groundtruth was provided by a pair of Magellan ProMark3 GPS units, which were used to produce post-processed differential GPS for the whole traverse. This measure of rover platform position allows us to confidently assess the accuracy of our motion estimates from VO.



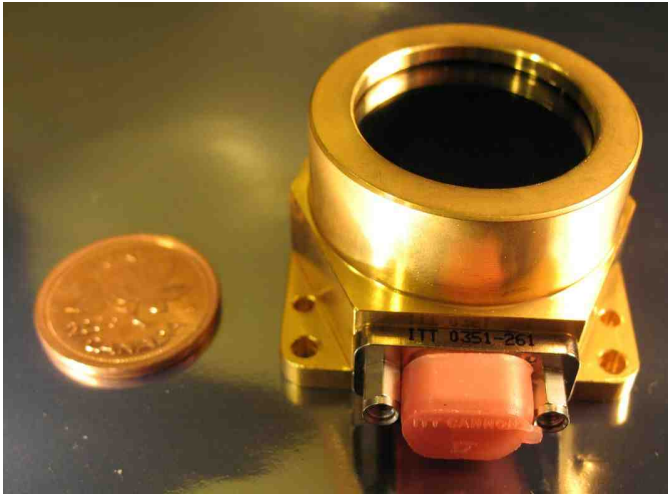


**Figure 7.** Sinclair Interplanetary SS-411 digital sun sensor.

### Hardware Configuration

The data set was collected using a pushcart platform outfitted with a suite of rover engineering sensors, as seen in Figure 8. Since our focus in this paper is on motion estimation, the unactuated nature of the platform is unimportant. The stereo camera was a Point Grey Research Bumblebee XB3 with a baseline of 24 cm and a  $70^\circ$  field of view, mounted approximately 1 m above the surface pointing downward by approximately  $20^\circ$ . Over the course of the 10 km traverse, the stereo camera acquired 49410 images, which have been processed to  $512 \times 384$  rectified greyscale images for these experiments. Color versions of some typical images from the data set are presented in Figure 4, further illustrating the Mars-like nature of the terrain. Keypoints were extracted and tracked in the images using a similar GPU SURF implementation as the one described by Furgale [7]. The inclinometer was a Honeywell HMR-3000, which weighs only 90 grams and uses a fluid tilt sensor to estimate the direction of gravity. Since the sensor directly outputs gravity vectors, the rover computer does not have to perform any expensive computation on these measurements.

The sun sensor used in these experiments is a Sinclair Interplanetary SS-411 digital sun sensor, as shown in Figure 7. It is a low-power, low-mass device designed for use on microsatellites, weighing in at only 30 grams. A linear pixel array is used to capture an image, which is then processed by an integrated microcontroller to output floating point sun vector measurements in the sensor frame [6]. Since the processing is done onboard by the sensor, producing sun vector measurements is of minimal computational cost to the rover computer. Additionally, the sensor monitors the quality of the detector images, rejecting poor quality images that can be caused by clouds or other factors. This produces intermittent gaps in the sun sensor data, which can subsequently affect our motion estimate. However, our VO framework is flexible enough to incorporate sun measurements when available and rely entirely on stereo vision when they are not.

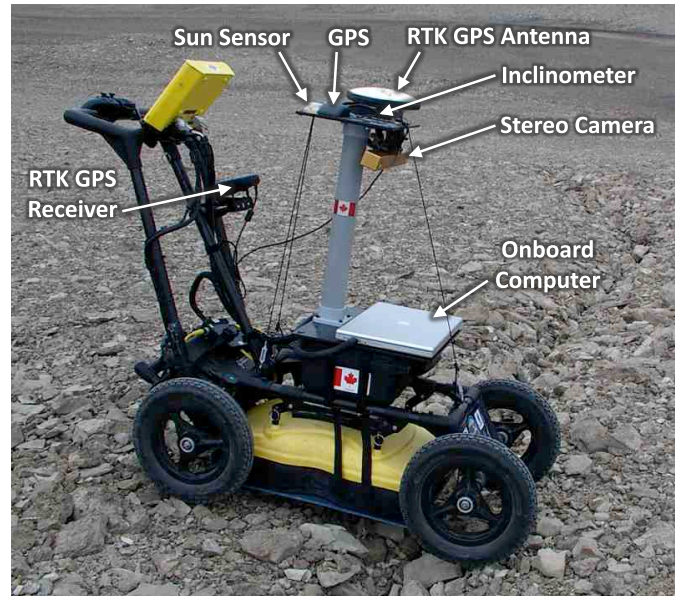


**Figure 8.** The pushcart rover platform at Devon Island.

## 5. EXPERIMENTAL RESULTS

We will now present the experimental results produced by running our algorithm, as previously outlined in Section 3, offline on the 10 km loop data set from Devon Island. Motion estimates were calculated for each of the 23 individual sections of the traverse, allowing us to illustrate statistical trends on a large set of data. Next, we focus in on one of the typical sections, to observe the properties of the motion estimate itself. Finally, we combined six of the sections together to produce an approximately 3 km long traverse, where we can better observe the superlinear nature of the error growth.

### Results for Individual Sections

In this section, we present the motion estimates for each of the 23 sections produced by visual odometry incorporating sun sensor and inclinometer measurements. We compare these results against the motion estimate produced using visual odometry only. As previously mentioned, for the purpose of accurate error reporting, we have aligned the first 50 m of each estimated path with groundtruth and then calculated the error on the remainder of the traverse. It is also important to note that some parameters in the algorithm required tuning, such as the sun sensor measurement covariance and a disparity threshold for the stereo keypoint measurements. These values were tuned to optimize performance on Section 0, and then those tuned parameters were retained for use with every other section. This procedure is similar to any field trial, in which parameters can be tuned based on a known set of data, and then tested experimentally in the field.

The results are summarized in Table 5, with the three-dimensional motion estimate error being expressed as a percentage of the total traversal distance. From these results, we observe that, statistically, the addition of sun sensor and in-

**Table 1.** XYZ error expressed as percentage of traversal distance for individual sections

Section	Distance (m)	VO (%)	VO-SS-Inc (%)
0	413	2.7	2.7
1	477	11.0	5.8
2	606	6.2	1.1
3	541	13.9	1.6
4	402	8.5	0.9
5	552	9.4	1.9
6	538	5.4	7.7
7	499	10.7	2.0
8	444	12.6	4.4
9	487	8.6	6.1
10	572	13.0	4.2
11	386	4.3	4.0
12	557	21.4	4.2
13	490	14.1	2.0
14	442	12.6	2.3
15	557	11.8	2.8
16	503	18.5	10.6
17	423	15.0	7.4
18	338	11.2	7.3
19	316	3.9	1.0
20	296	5.7	1.2
21	170	2.8	3.2
22	124	3.3	1.6

clinometer measurements produces a much better motion estimate, often dramatically so. The most striking thing about this improvement is that it comes at a very minimal cost. The rover needs not perform any computation to acquire the measurement vectors, and since there are many more stereo key-points than sun or gravity vectors, the additional cost to bundle adjustment is almost negligible. A simple timing analysis on our code showed that including the sun sensor and inclinometer measurements increased the computation time by approximately 0.3%.

The effect of the sun sensor and inclinometer is further illustrated when the XYZ (i.e., Euclidean) error of the motion estimates is plotted as a function of distance traversed. Figure 9(a) shows that the error of visual odometry grows superlinearly with distance. As previously discussed, this is because small orientation errors become amplified into large position errors over long distances. In contrast, Figure 9(b) shows that sun sensor and inclinometer measurements limit the error growth significantly on a large set of unique traverses. The constant orientation corrections from the sun sensor and inclinometer keep the platform attitude close to true, preventing the amplification of errors. Note that the error curves are noisier for the corrected version of visual odometry than the uncorrected. This extra noise was contributed by our inclinometer data, which proved to be extremely noisy due to a number of factors. The terrain was often quite rough, the pushcart rover platform did not have any sort of suspension, and the sensor head was mounted on a tall mast that was

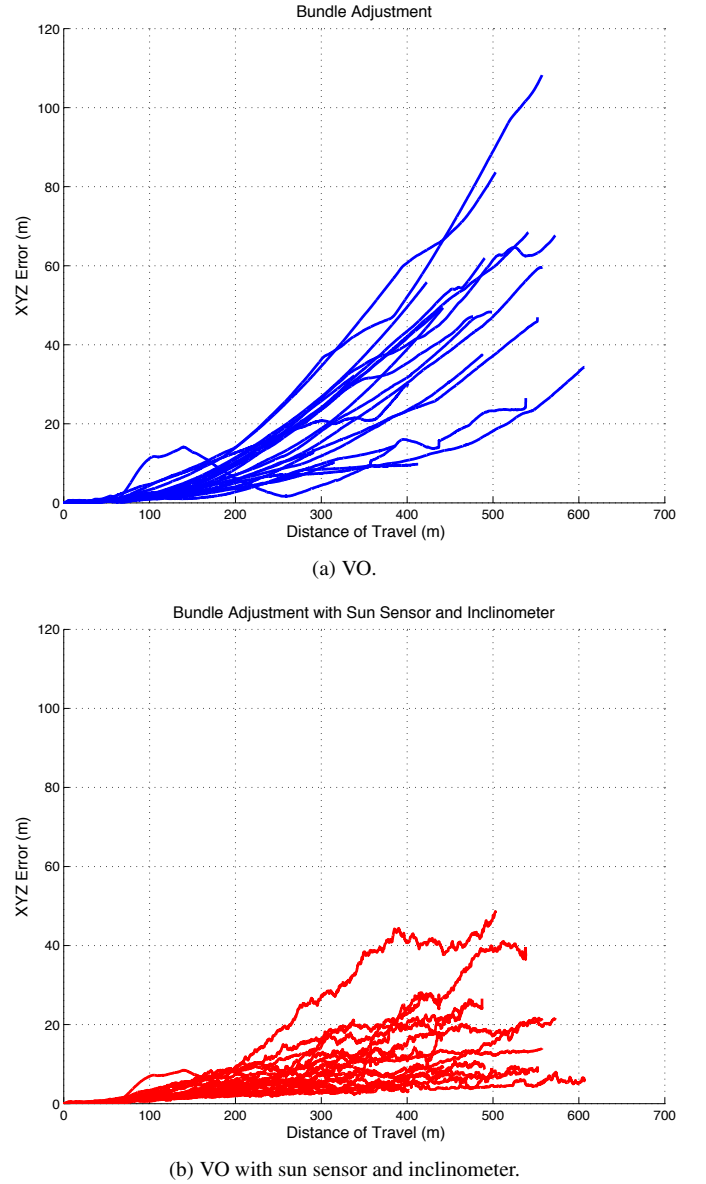
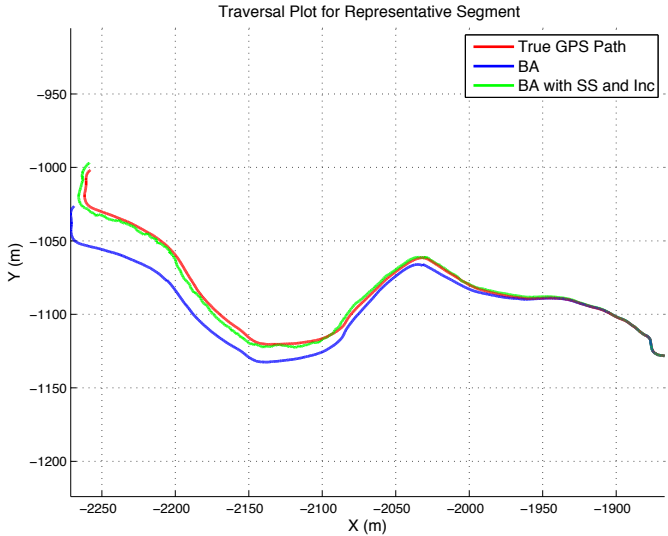
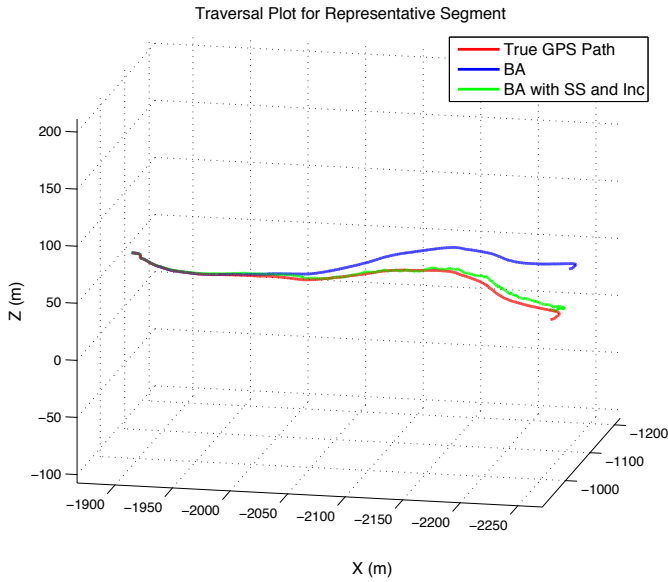


**Figure 9.** XYZ error as a function of distance for all individual traverses.

susceptible to vibrations. This produced a shaking motion of the inclinometer as the cart was pushed, causing the bubble tilt sensor to produce noisy measurements of the inclination. We suspect that this noise issue could be resolved by stopping the rover platform periodically to collect sun sensor and inclinometer measurements, which is more in line with MER procedures. This mode of operation was not feasible for our field trials, however, as we were required to push the cart continuously in order to complete the 10 km traverse within a limited time frame. Other possible solutions might include a more stable inclinometer, a rover platform with a proper suspension, smoothing the inclinometer data, or using a multiframe bundle adjustment approach to visual odometry.



(a) Top view.



(b) Angled view.

**Figure 10.** Multiple views of Segment 7 traverse with motion estimates.

In terms of the specific contributions of the sun sensor and inclinometer, the sun sensor will mainly provide information about the vehicle heading, and the inclinometer largely the pitch and roll. However, both sensors provide some measure of the full attitude of the rover. This is because, over the course of a traverse, the ground undulates and the sun moves in the sky, so the sensors will be measuring a continuous sequence of non-parallel vectors. In our experiments, we have found that the combination of both sensors greatly outperforms the use of either the sun sensor or the inclinometer alone. This is not only due to the fact that we are obtaining two distinct sets of vectors in nearly perpendicular directions, but we can also apply more frequent corrections.

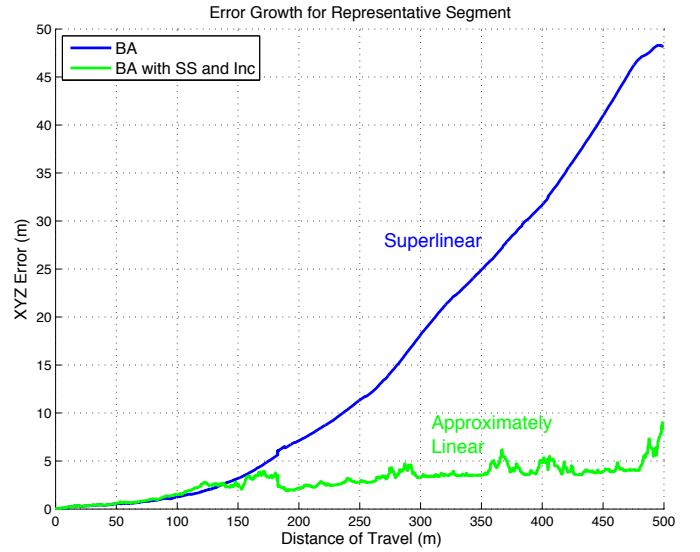


**Figure 11.** Error growth as a function of distance for the Segment 7 traverse.

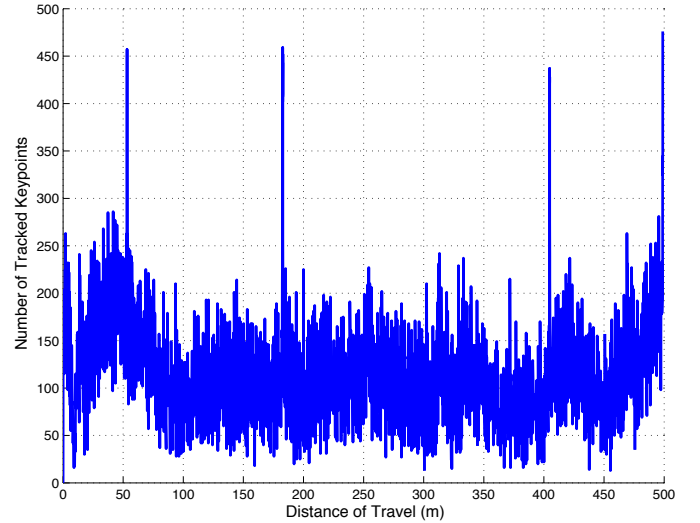


**Figure 12.** Number of stereo keypoints tracked as a function of distance for the section 7 traverse.

#### *Detailed Results for a Specific Traverse*

In the previous section, we showed on a large set of individual traverses the statistical error improvement of VO with sun sensor and inclinometer measurements included. However, it is beneficial to focus in on a single typical example of these traverses, in order to glean some finer detail. For this paper, we will focus in on Section 7, which demonstrates a typical error improvement. In order to visualize how our algorithm affects the motion estimate itself, we have presented the Section 7 traverse and motion estimates from multiple viewpoints in Figure 10. We observe that the heading error is greatly reduced, due to the corrections of the sun sensor, as well as the pitch error, due to the corrections of the inclinometer. This is further illustrated in Figure 11, which shows how the absolute orientation has restricted the error growth. We note

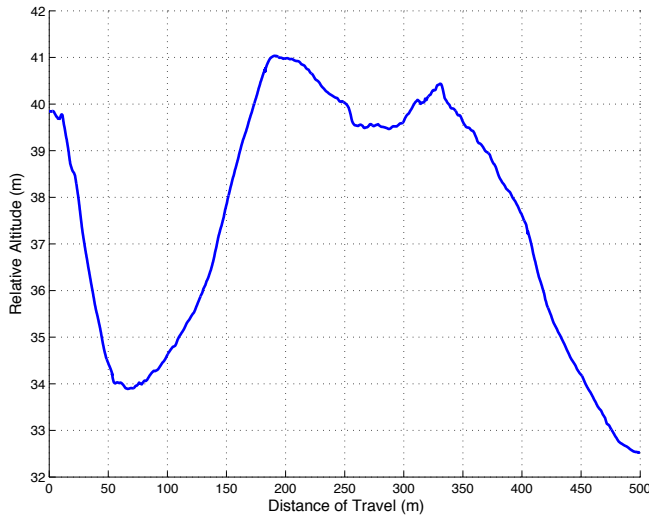


**Figure 13.** Altitude, relative to start of 10 km loop, as a function of distance for the section 7 traverse.

that the corrected visual odometry estimate is not necessarily better at shorter distances, due to the effect of the noisy inclinometer data. However, over longer distances, the restricted of the error growth makes a large improvement in the error. Once again, the significant accuracy improvements provided by the sun sensor and inclinometer are achieved with negligible additional computational cost. For additional detail, Figures 12 and 13 have also been included, showing the number of tracked stereo keypoints and the rover altitude as functions of path length, respectively.

### 3 Kilometer Traverse

Since the error of visual odometry grows superlinearly with distance, we should see even greater improvements over longer range traverses. To demonstrate this, we concatenated the measurements from the first six sections of the ten kilometre loop to produce a single, 2991 m traverse. As expected, the sun sensor and inclinometer measurements produce a dramatically better motion estimate over the approximately 3 km distance, as seen in Figure 14. At the end of the traverse, the XYZ error using corrected visual odometry was only 1.1% of the total distance travelled.

## 6. CONCLUSIONS

In this paper, we have presented a novel algorithm for incorporating sun sensor and inclinometer measurements directly into the visual odometry solution using bundle adjustment. Through rigorous testing on 10 kilometres of data from a planetary analog environment, we demonstrated that these absolute orientation measurements greatly restrict the error growth of the motion estimate, especially over long traversal distances. For future planetary exploration missions, long range autonomous driving may expand the capabilities and science-gathering abilities of rovers. While the use of a magnetic compass is not possible, the inclusion of sun sensor and inclinometer measurements is able to keep the rover accu-

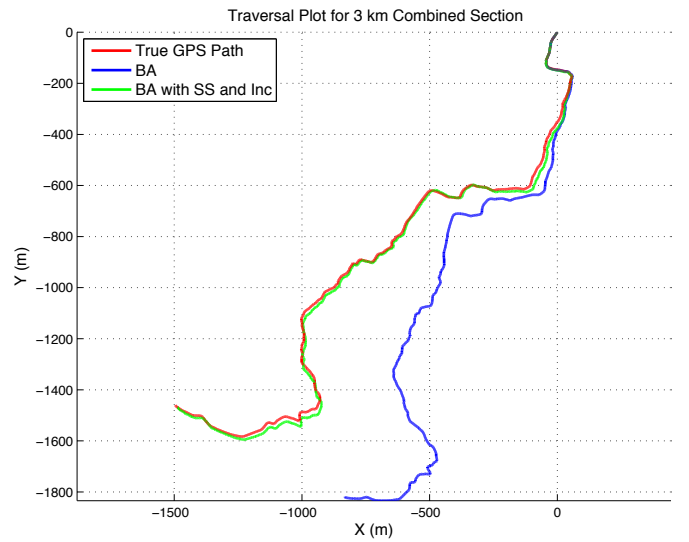


**Figure 14.** True path and motion estimates for the combined 3 km traverse.

ately on course during these traverses. Importantly, incorporating these additional measurements comes at a minimal cost in terms of power, weight, and computation. In other words, one could easily improve an existing visual odometry system with minimal effort and cost by adding and integrating these two sensors.

### Future Work

There are a number of possible extensions of the work presented in this paper, which we plan to explore in future publications. One of the most interesting applications is using sun sensor and inclinometer measurements to reduce the computational requirements of visual odometry. Our implementation is already fairly lean, as we do not use a multiframe approach, and our additional measurements are very inexpensive. However, since adding absolute orientation information greatly improves our motion estimate, this approach may allow an increase in the driving distance between VO images while maintaining the accuracy of a conventional VO system. This reduces the total computation per distance travelled, which would be particularly beneficial for computationally-constrained missions such as MER. We would like to examine how far we can increase the distance between subsequent images while maintaining an appropriate level of accuracy. It would also be of interest to closely examine the individual contributions of the sun sensor and inclinometer, to establish in which scenarios the sensors are most beneficial.

## ACKNOWLEDGMENTS

The authors would like to thank Mr. Doug Sinclair of Sinclair Interplanetary for the donation of a SS-411 Digital Sun Sensor. Funding for this work was provided in part by the Natural Sciences and Engineering Research Council (NSERC) of Canada. Funding for our field trials on Devon Island was provided by the Canadian Space Agency's Canadian Analogue

Research Network (CARN) program. Thanks to the Mars Institute and the Houghton-Mars Project for providing infrastructure on Devon Island. The authors are grateful to the members of the communities of Resolute Bay, Grise Fjord, and Pond Inlet who acted as guides on Devon Island.

## REFERENCES

- [1] T D Barfoot, J R Forbes, and P T Furgale. Pose estimation using linearized rotations and quaternion algebra. *Acta Astronautica*, 2010. doi:10.1016/j.actaastro.2010.06.049.
- [2] T D Barfoot, P T Furgale, B E Stenning, P J F Carle, J P Enright, and P Lee. Devon Island as a proving ground for planetary rovers. In *Proceedings of the Symposium on Brain, Body, and Machine*, a “Celebration of 25 Years of Research Excellence at the McGill Centre for Intelligent Machines”, to appear, Montreal, Quebec, 10-12 November 2010.
- [3] D. C. Brown. A solution to the general problem of multiple station analytical stereotriangulation. Technical report, RCP-MTP Data Reduction Technical Report No. 43, Patrick Air Force Base, Florida (also designated as AFMTC 58-8), 1958.
- [4] A.R. Eisenman, C.C. Liebe, and R. Perez. Sun sensing on the Mars exploration rovers. In *Aerospace Conference Proceedings, 2002. IEEE*, volume 5, pages 5–2249–5–2262 vol.5, 2002.
- [5] J Enright, P Furgale, and T D Barfoot. Sun sensing for planetary rover navigation. In *Proceedings of the IEEE Aerospace Conference*, Big Sky, MT, 7-14 March 2009.
- [6] J Enright and D Sinclair. Algorithm enhancements for the SS-411 digital sun sensor. In *Proceedings of the 21st Annual AIAA/USU Conference on Small Satellites*, Logan, Utah, 2007.
- [7] P T Furgale and T D Barfoot. Visual teach and repeat for long-range rover autonomy. *Journal of Field Robotics*, special issue on “Visual mapping and navigation outdoors”, 27(5):534–560, 2010.
- [8] P T Furgale, P Carle, J Enright, and T D Barfoot. The Devon Island rover navigation dataset. Submitted to the *International Journal of Robotics Research* on October 4, 2010. Manuscript # IJR-10-0896.
- [9] C. Harris and M. Stephens. A combined corner and edge detection. In *Proceedings of The Fourth Alvey Vision Conference*, pages 147–151, 1988.
- [10] Andrew Howard. Real-time stereo visual odometry for autonomous ground vehicles. In *Intelligent Robots and Systems, 2008. (IROS 2008). 2008 IEEE/RSJ International Conference on*, pages 3946–3952, 2008.
- [11] P C Hughes. *Spacecraft Attitude Dynamics*. John Wiley & Sons, New York, 1986.
- [12] Kurt Konolige, Motilal Agrawal, and Joan Solà. Large scale visual odometry for rough terrain. In *Proc. International Symposium on Research in Robotics (ISRR)*, November 2007.
- [13] M. Maimone, Y. Cheng, and L. Matthies. Two years of visual odometry on the Mars exploration rovers. *Journal of Field Robotics*, 24(3):169–186, 2007.
- [14] L. Matthies. Stereo vision for planetary rovers - stochastic modeling to near real-time implementation. *International Journal of Computer Vision*, 8(1):71–91, 1992.
- [15] L. Matthies, M. Maimone, A. Johnson, Y. Cheng, R. Willson, C. Villalpando, S. Goldberg, A. Huertas, A. Stein, and A. Angelova. Computer vision on Mars. *International Journal of Computer Vision*, 75(1):67–92, 2007.
- [16] L. Matthies and Steven Shafer. Error modeling in stereo navigation. *IEEE Journal of Robotics and Automation*, RA-3(1):239 – 250, June 1987.
- [17] C. Mei, G. Sibley, M. Cummins, P. Newman, and I. Reid. RSLAM: A system for large-scale mapping in constant-time using stereo. *International Journal of Computer Vision*, pages 1–17, 2010. Special issue of BMVC.
- [18] Hans Moravec. Obstacle avoidance and navigation in the real world by a seeing robot rover. Technical Report CMU-RI-TR-80-03, Robotics Institute, Carnegie Mellon University, September 1980.
- [19] David Nister, Oleg Naroditsky, and James Bergen. Visual odometry for ground vehicle applications. *Journal of Field Robotics*, 23(1):3, 2006.
- [20] C. F. Olson, L. H. Matthies, M. Schoppers, and M. W. Maimone. Rover navigation using stereo ego-motion. *Robotics and Autonomous Systems*, 43(4):215–229, 2003.
- [21] A. Trebi-Ollennu, T. Huntsberger, Yang Cheng, E.T. Baumgartner, B. Kennedy, and P. Schenker. Design and analysis of a sun sensor for planetary rover absolute heading detection. *Robotics and Automation, IEEE Transactions on*, 17(6):939–947, Dec 2001.
- [22] R. Volpe. Mars rover navigation results using sun sensor heading determination. In *Intelligent Robots and Systems, 1999. IROS ’99. Proceedings. 1999 IEEE/RSJ International Conference on*, volume 1, pages 460–467 vol.1, 1999.
- [23] Brian Wilcox and Tam Nguyen. Sojourner on Mars and lessons learned for future planetary rovers. In *Proceedings of the 28th SAE International Conference on Environmental Systems (ICES)*, Danvers, Massachusetts, 1998.



## BIOGRAPHY



**Andrew Lambert** received his BEng (2009) from McMaster University (Mechanical Engineering) and is now a MASc Student in the Autonomous Space Robotics Lab at the University of Toronto Institute for Aerospace Studies (UTIAS). His research focuses on techniques for improving efficiency and reducing bias in visual odometry.



**Paul Furgale** is an IEEE student member. He received his BASc (2006) from the University of Manitoba (Computer Science) and is now a PhD Candidate in the Autonomous Space Robotics Lab at the University of Toronto Institute for Aerospace Studies (UTIAS). His research interests include computer vision and localization technology for rovers in GPS-denied environments.



**Timothy D. Barfoot** is an IEEE member. He holds a B.A.Sc. degree (1997) from the University of Toronto in engineering science (aerospace option), and a Ph.D. degree (2002) from the University of Toronto Institute for Aerospace Studies (UTIAS) in aerospace engineering. He is currently an Assistant Professor at UTIAS, where he leads the Autonomous Space Robotics Lab (ASRL). Before joining UTIAS, he worked at MDA Space Missions in the Controls & Analysis Group on applications of mobile robotics to space exploration and underground mining. Dr. Barfoot is a Canada Research Chair (Tier II) in Autonomous Space Robotics and a Professional Engineer in Ontario, Canada.



**John Enright** holds a BASc (1997) from the University of Toronto (Engineering Science: Aerospace) and a MS (1999) and a PhD (2002) from MIT in Aerospace Systems. He is currently an Associate Professor in Aerospace Engineering at Ryerson University in Toronto. Having joined the faculty at Ryerson University in 2003, he is now the Principal Investigator of the Space Avionics and Instrumentation Laboratory (SAIL). While at MIT (1999-2003), he led the software development for the SPHERES flight project, and the GFLOPS real-time spacecraft simulation testbed. His research interests include spacecraft avionics and sensor processing, systems engineering and flight software. Dr. Enright is a member of the AIAA, CASI, and the IEEE.